

SEARCH FOR LONG-LIVED RESONANCE
DECAYING TO A DILEPTON PAIR IN pp
COLLISIONS AT $\sqrt{s} = 13$ TEV WITH
THE ATLAS DETECTOR

DISSERTATION

Presented in Partial Fulfillment of the Requirements for the Degree Doctor of
Philosophy in the Graduate School of The Ohio State University

By

Siinn Che, B.S., M.S.

Graduate Program in Physics

The Ohio State University

2018

Dissertation Committee:

Professor K.K. Gan, Advisor

Professor Richard Kass

Professor Junko Shigemitsu

Professor Fengyuan Yang

© Copyright by
Siinn Che
2018

ABSTRACT

A search for long-lived neutral massive particle decaying to a $\mu\mu$, ee , or $e\mu$ pair is presented using the ATLAS detector with 32.8 fb^{-1} of pp collisions at $\sqrt{s} = 13 \text{ TeV}$ at the LHC. Upper limits are presented on the production cross section times branching ratio for resonances decaying to a lepton pair. Also presented is the detection efficiency as a function of p_T and η for a resonance with mass of $0.1\text{--}2.0 \text{ TeV}$ and lifetime ($c\tau$) of $100\text{--}500 \text{ mm}$.

Dedication

some more text

ACKNOWLEDGMENTS

I would like to thank my parents for their endless support and love. Also, I would like to thank Prof. K.K. Gan for his guidance and support throughout my graduate career. I won't forget the cheese.

Table of Contents

	Page
Abstract	ii
Dedication	iii
Acknowledgments	iv
List of Figures	vii
List of Tables	viii

Chapters

1 Introduction and Theory	1
1.1 The Standard Model	1
1.1.1 Fundamental Particles and Interactions	1
1.2 Beyond the Standard Model	3
1.2.1 Z' from the extension of the Standard Model	3
1.2.2 Long-lived Z' Discovery Mode at the LHC	4
2 The ATLAS Experiment at the LHC	6
2.1 The Large Hadron Collider	6
2.2 The ATLAS detector	7
2.2.1 The Inner Detector	7
2.2.2 The Calorimeters	10
2.2.3 The Muon Spectrometer	12
2.2.4 The ATLAS Magnet	14
2.3 The ATLAS Trigger System	14
2.3.1 Level 1 Trigger	15
2.3.2 High Level Trigger	16
3 Z' Reconstruction	17
3.1 Track Reconstruction in the Inner Detector	17
3.1.1 Standard Tracking	17
3.1.2 Large Radius Tracking	19

3.2	Electron Reconstruction	19
3.3	Muon Reconstruction	20
3.4	Secondary Vertex Reconstruction	20
4	Analysis Overview	22
6	Data and MC samples	28
6.1	Data samples	28
6.2	MC samples	29
6.2.1	Signal samples	29
6.2.2	Background MC samples	30
6	Data and MC samples	28
6.1	Data samples	28
6.2	MC samples	29
6.2.1	Signal samples	29
6.2.2	Background MC samples	30
7	Background Estimation	33
7.1	Random-Crossing Background	33
8	Systematic Uncertainties	34
8.1	Systematics in Vertexing and Tracking	34
	Bibliography	35
 Appendices		
A	Truth-level p_T and η distributions of Signal MC samples	39

List of Figures

Figure	Page
2.1 An illustration of the LHC accelerators and the four main experiments.	7
2.2 The ATLAS detector and the sub-detector systems.	8
2.3 The ATLAS calorimeter system.	10
2.4 The ATLAS Muon Spectrometer	12
2.5 Layout of the ATLAS Trigger and data acquisition system in Run 2.	15
3.1 Illustration of detector hits and reconstructed tracks in the Inner Detector. The bright colors represent the detector hits associated with reconstructed tracks [1].	18
3.2 Important vertex topologies in pp collisions: primary, pile-up, and secondary vertices.	21
6.1 The representative plots of truth-level (a) p_T and (b) η distributions of Z' , and (c), (d) are the corresponding distributions for the signal muons. The signal MC samples are generated with $m = 500, 1000$ GeV, and $c\tau = 100$ mm.	31
6.1 The representative plots of truth-level (a) p_T and (b) η distributions of Z' , and (c), (d) are the corresponding distributions for the signal muons. The signal MC samples are generated with $m = 500, 1000$ GeV, and $c\tau = 100$ mm.	31

List of Tables

Table		Page
1.1	The fundamental fermions and their electric charge Q and masses.	2
1.2	Gauge bosons and their associated fields and masses.	3
3.1	Important track selection in the standard and the large radius tracking algorithms.	18
3.2	Track requirements for secondary vertex reconstruction.	21
6.1	Dataset used in DRAW_RPVLL, DAOD_RPVLL, and DAOD_SUSY15 format.	29
6.2	Mass, lifetime, and DID of the signal MC samples.	30
6.3	Background MC samples used in the study of random-crossing background and in the estimation of tracking and vertexing systematic uncertainty.	32
6.1	Dataset used in DRAW_RPVLL, DAOD_RPVLL, and DAOD_SUSY15 format.	29
6.2	Mass, lifetime, and DID of the signal MC samples.	30
6.3	Background MC samples used in the study of random-crossing background and in the estimation of tracking and vertexing systematic uncertainty.	32

Chapter 1

INTRODUCTION AND THEORY

In this chapter, the theoretical background and motivation for the search for new physics with long-lived particles are presented. In Section 1.1, an overview of the Standard Model of particle physics is presented. In Section 1.2 the theories beyond the Standard Model that predict new long-lived gauge bosons and the potential discovery mode of the new particles are discussed.

1.1 The Standard Model

The Standard Model (SM) [2] of particle physics has been the most successful theory in modern physics that describes the known fundamental particles and their interactions. The SM is a gauge theory based on $SU(3) \otimes SU(2) \otimes U(1)$ symmetry group. The symmetry group describes three fundamental interactions, quantum chromodynamics (QCD), quantum electrodynamics (QED), and weak interactions, which arises from the requirement of local gauge invariance. Gravity, the fourth fundamental interaction, is not incorporated in the SM because the gravitational force is much weaker than the electroweak or strong forces. All known matters are described by spin $\frac{1}{2}$ fermions, and the interactions between the fermions are mediated by spin 1 gauge bosons. Fermions acquire mass by interacting with the Higgs field H via spontaneous symmetry breaking [3].

1.1.1 Fundamental Particles and Interactions

The elementary particles in the SM can be divided into two groups, fermions and bosons.

Fermions are spin $\frac{1}{2}$ particles that constitute the building blocks of matter, and they

can be divided into two groups, leptons and quarks, depending on the coupling to gluons. Leptons are colorless particles that do not interact through the strong force, and quarks are subject to the strong force due to color charges. There are three generations of leptons and quarks in increasing mass, and each generation consists of two leptons (electric charge 1 or 0) and two quarks (electric charge $\frac{2}{3}$ or $-\frac{1}{3}$). Quarks and charged leptons interact through the electroweak interaction while neutrinos only experience weak interaction. Fermions are described as quantum fields with *left-handed* or *right-handed* chirality, and only *left-handed* fermions and *right-handed* antifermions are subject to the weak interaction. This phenomenon is known as CP-violation [4]. Quarks are not observed as free particles due to *color confinement* [5], but they are only observed in color-neutral bound states, called *hadrons*. There are two types of hadrons: *mesons* and *baryons*. Mesons are composite particles with quark and anti-quark pair, and baryons are composed of three quarks. The elementary fermions are summarized in Table 1.1.

	Generation			Q	Mass (MeV)		
	1 st	2 nd	3 rd				
Leptons	ν_e	ν_μ	ν_τ	0	0	0	0
	e	μ	τ	-1	0.511	105.7	1777
Quarks	u	c	t	$+2/3$	2.3	1275	173070
	d	s	b	$-1/3$	4.8	95	4180

Table 1.1: The fundamental fermions and their electric charge Q and masses.

The fundamental interactions are described by gauge bosons, spin 1 particles that are generated by the symmetry groups in the SM. Gluon fields are generated by $SU(3)$ group, and quanta of gluon fields produce massless gluons that mediate strong forces. The group $SU(2) \otimes U(1)$ generates gauge fields W_μ^a ($a = 1, 2, 3$) and B_μ which mediate electroweak force. The physical observable gauge bosons W^\pm , Z , and photon are created by the mixing of these gauge fields as described in Eq. 1.1

$$\begin{aligned}
W_\mu^\pm &= (W_\mu^1 \mp iW_\mu^2)/\sqrt{2} \\
Z_\mu &= \cos \theta_W W_\mu^3 - \sin \theta_W B_\mu \\
A_\mu &= \sin \theta_W W_\mu^3 + \cos \theta_W B_\mu
\end{aligned} \tag{1.1}$$

where θ_W is the weak mixing angle.

Photon and gluons are massless, and W^\pm and Z bosons gain masses through the Higgs

mechanism [6] via spontaneous symmetry breaking. In the Higgs mechanism, an additional complex scalar field, called Higgs field, is introduced with $SU(2)$ symmetry, and because the Higgs potential has non trivial vacuum expectation value, the symmetry of the ground state is spontaneously broken, leading to a massive scalar particle with spin 0, known as Higgs boson.

All elementary particle have associated anti-particles with the same property but with opposite charge. Therefore, neutral particles such as photon, Z , gluons and neutrinos are identical to its own anti-particles. The gauge bosons and their associated fields, and masses are summarized in Table 1.2

Symmetry	Gauge boson	Gauge Field	Q	Mass (GeV)
$SU(2) \otimes U(1)$	γ	A_μ	0	0
	Z	Z_μ	0	91.2
	W^\pm	W_μ^\pm	± 1	80.4
$SU(3)$	g	g_μ^a	0	0

Table 1.2: Gauge bosons and their associated fields and masses.

1.2 Beyond the Standard Model

Although the SM has been the most successful theory at explaining fundamental particles and their interactions, there are several experimental observations and phenomena in nature that are not fully explained by the SM. These phenomena include gravity [7], hierarchy problem [8] [9], dark matter [10] [11] [12], neutrino oscillations [13] [14], and matter-antimatter asymmetry [15] [16].

Many Beyond the Standard Model (BSM) theories have been proposed to explain these unexplained phenomena, and they predict the existence of new particles. In particular, theories such as Hidden Valley [17] [18], R-parity violation [19] [20], and Z' models with neutrinos [21] predict the existence of weakly-coupled, neutral gauge boson at the weak scale. The new gauge boson is called Z' due to the similarity to the standard Z boson.

1.2.1 Z' from the extension of the Standard Model

The new weakly-coupled gauge boson can be added to the SM by including a additional $U(1)'$ symmetry to the existing $SU(3) \otimes SU(2) \otimes U(1)$ symmetry. The spontaneous breaking of

the $U(1)'$ symmetry, similar to the electroweak symmetry breaking, produces the new gauge boson, Z' [22]. The mechanism through which the new symmetry is added to the SM varies by theories. Nonetheless, the Z' boson has two sets of parameters defining its property: the couplings to the SM particles and the energy scale at which the $U(1)'$ symmetry is broken. The former defines the lifetime, $c\tau$, of the particle while the latter defines the mass of the particle.

In one case, Z' can have the same couplings to fermions as the SM Z boson, and the particle is called *sequential Z'* [23]. There have been several searches for the sequential Z' [24] [25] [26], and although the sequential Z' provides useful reference for some theories, it will not be considered in this thesis as the main focus of the analysis is the long-lived particles.

In other case, the Z' can have very small couplings to the SM particles such that the particle have a finite lifetime compatible with the detector volume at the ATLAS experiment. This metastable particle is called the *long-lived Z'* , and this model will be used as a basis of this thesis.

1.2.2 Long-lived Z' Discovery Mode at the LHC

The long-lived Z' can be directly produced and discovered from pp collisions at the Large Hadron Collider (LHC). The primary discovery mode for the long-lived Z' is via the Drell-Yan (DY) production of a dilepton resonance, $pp \rightarrow Z' \rightarrow \ell^+ \ell^-$ where $\ell = e$ or μ [27].

The cross section for Z' decaying to two leptons ($pp \rightarrow Z' \rightarrow \ell\ell\bar{\ell}\ell$) is simply given by Eq. 1.2 [28],

$$\sigma_{Z'}^{\ell\ell} = \sigma_{Z'} B_{\ell\ell} = \frac{N_{\ell\ell}}{\mathcal{L}_I} \quad (1.2)$$

where $\sigma_{Z'}$ is the production cross section of Z' , $B_{\ell\ell} = \Gamma_f/\Gamma_{Z'}$ is the branching ratio of Z' into $\ell\ell\bar{\ell}\ell$, and $N_{\ell\ell}$ is the number of $\ell\ell\bar{\ell}\ell$ produced for integrated luminosity \mathcal{L}_I . Therefore, if Z' is light enough to be produced at the LHC, the sensitivity to detect Z' depends on luminosity, the production cross section, and the branching ratio into a particular channel.

Long-lived particles naturally have small width ($\tau_0 = \hbar/\Gamma$), and the detectable mass range and lifetime of Z' is constrained by the center of mass energy (13 TeV in Run II) and the detector volume ($\sim O(1m)$).

Other potential discovery channels exist in searches for Z' such as $Z' \rightarrow \tau^+ \tau^-$ and

hadronic decay, $Z' \rightarrow jj$ where $j = \text{jet}$ although these decay modes are more experimentally difficult to detect due to the irreducible QCD background. But the search for long-lived Z' through a dilepton resonance is particularly interesting due to its clean final signature and low backgrounds from the SM.

More rare decays are also possible such as $Z' \rightarrow Vf_1\bar{f}_2$ where $V = W, Z$ or Z' decaying to two bosons, but these rare decays will be extremely difficult to detect due to the small branching ratio [28].

Chapter 2

THE ATLAS EXPERIMENT AT THE LHC

The ATLAS experiment is one of the four major experiments at the LHC at The European Organization for Nuclear Research (CERN). The ATLAS experiment is designed as a general-purpose particle experiment, together with the CMS experiment. In Section 2.1, a brief description of the LHC is given, and in Section 2.2, the ATLAS detector and its sub-detector systems are described.

2.1 The Large Hadron Collider

The LHC is the world's largest synchrotron accelerator and pp collider located underneath the CERN campus near Geneva, Switzerland. The LHC's circular beam pipes are 27 km in circumference, and two beams of protons are accelerated in opposite direction producing pp collisions at $\sqrt{s} = 13$ TeV in Run II. Separate magnet systems are used to direct proton beams in each direction.

There are 8 interaction regions (IRs) at which two proton beams cross, and protons beams are injected into the LHC from two IRs. Before protons are injected to the LHC, they undergo a multi-stage acceleration by several accelerators [29]: a linear accelerator (LINAC2), the Proton Synchrotron Booster, the Proton Synchrotron (PS), and the Super Proton Synchrotron (SPS). The proton beams are accelerated up to 450 GeV when they are injected to the LHC with a 25 ns bunch spacing in Run II. There are more than 10^{11} protons in each bunch, and the large number of protons in each bunch results in multiple collisions per bunch crossing, known as *pile-up*. In 2016, the mean number of interactions per bunch crossing was $\langle\mu\rangle = 24.9$.

The four main experiments at CERN are distributed around the LHC at collision points.

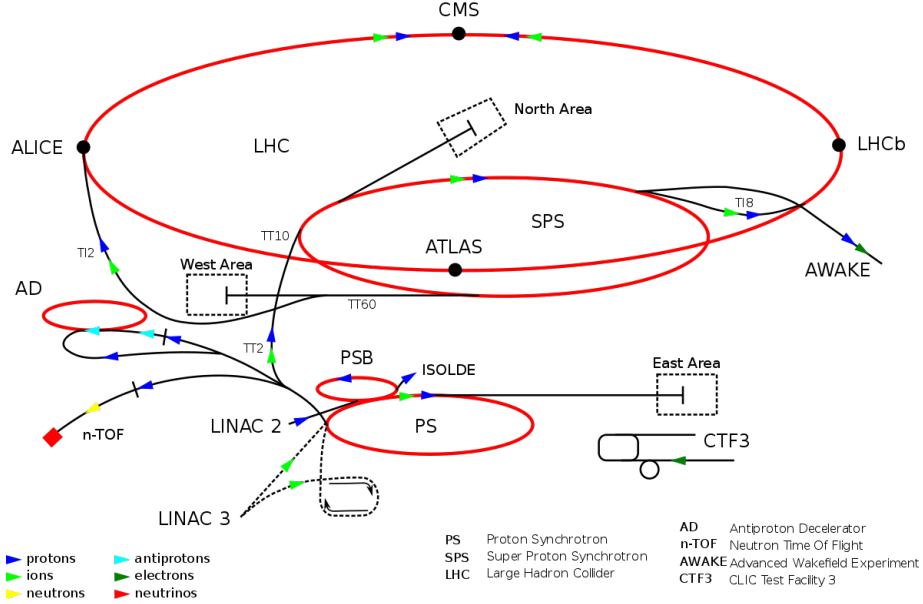


Figure 2.1: An illustration of the LHC accelerators and the four main experiments.

Two experiments, ATLAS and CMS, are designed as general purpose experiments, and A large Ion Collider Experiment (ALICE) and the Large Hadron Collider beauty (LHCb) are designed to study strong interaction using heavy ion collisions and the matter-antimatter asymmetry using b quarks, respectively. Figure 2.1 shows the four main experiments and the accelerators at the LHC.

2.2 The ATLAS detector

The ATLAS detector is a multi-purpose detector designed to investigate a wide range of physics, including the search for the Higgs boson in Run I and many searches beyond the SM. The detector measures 46 m long, 25 m in diameter, and it has three main layers of sub-detectors to detect particles created from pp collisions at the Interaction Point (IP). Figure 2.2 shows the ATLAS detector and the sub-detector systems: the Inner detector, the electromagnetic and hadronic calorimeters, and the muon spectrometer. In this section, the sub-detectors and the magnet system of the ATLAS detector are discussed.

2.2.1 The Inner Detector

The Inner Detector (ID) is a particle tracker designed to provides information about transverse momentum, charge, and trajectory of charged particles. It consists of cylindrical barrels

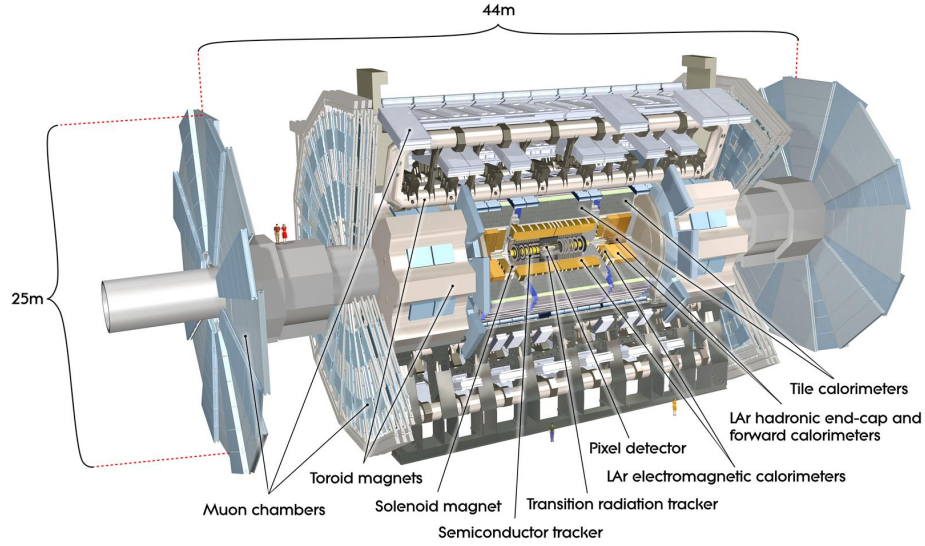


Figure 2.2: The ATLAS detector and the sub-detector systems.

and two end-cap disks from three sub-detectors centered around the IP. The ID covers the pseudo-rapidity region up to $|\eta| < 2.5$. Pseudo-rapidity describes the angle of a particle with respect to the z axis as defined in Eq. 2.1, and it is particularly useful because the quantity is Lorentz invariant under a boost along the z axis.

$$\eta = -\ln\left(\tan\left(\frac{\theta}{2}\right)\right) \quad (2.1)$$

The detector is placed under a 2 T magnetic field generated by the superconducting solenoid magnets, and the magnetic field is used to alter trajectories of charged particles. The curvature of the trajectory provides the transverse momentum and the charge of a particle, and the spatial information is used to reconstruct primary and secondary vertices.

The sub-detectors of the ID, the Pixel tracker, the semiconductor tracker (SCT), and the transition radiation tracker (TRT), are discussed in the following sections.

Pixel Detector

The Pixel detector is a semiconductor detector in the innermost part of the ATLAS tracking system. The detector consists of 4 concentric layers of barrel detectors and 3 disk detectors at each end-cap region. The barrels and disks are made of a rectangular Pixel modules containing $50 \times 400 \mu\text{m}^2$ pixels ($50 \times 250 \mu\text{m}^2$ for the IBL) [30]. As a charged particle traverse

through pixels, the currents generated by ionizing electrons are measured and registered as hits. The pixels provide spatial information with resolution of $\sim 8\text{ }\mu\text{m}$ in radial direction and $\sim 75\text{ }\mu\text{m}$ in the beam axis, and the information is used for momentum measurements as well as reconstruction of primary and secondary vertices. Several upgrades had been performed for Run 2 including the installation of the Insertable B-Layer (IBL) [31] to maintain and improve the performance of the ATLAS detector under increasing pile-up.

Semi-conductor Tracker

The Semi-Conductor Tracker (SCT) is the next tracking system following the Pixel detector. Similar to the Pixel detector, the SCT consists of 4 layers of barrel detectors and 9 disk detectors at each end-cap region. Each barrel/disk is made of SCT modules containing double-sided silicon strips, measuring $80\text{ }\mu\text{m}$ wide and 12 cm long¹. Strips are positioned parallel (perpendicular) to the beam axis in the barrel (end-cap) region. Because a single strip can only provide spatial information in $(r-\phi)$ direction in barrel and $(z-\phi)$ direction in end-cap region, double-sided strips are displaced by a relative angle of 40 mrad to provide three-dimensional spatial measurements of charged particles. The SCT has a spatial resolution of $17\text{ }\mu\text{m}$ in radial direction and $580\text{ }\mu\text{m}$ in z direction. The information collected by the SCT is used for transverse momentum measurement and reconstruction of vertices.

Transition Radiation Tracker

The Transition Radiation Tracker (TRT) is the outermost tracking system in the ID, covering the region up to $|\eta| < 2.0$. The TRT barrel region is covered by 52,544 straw tubes aligned parallel to the beam axis. The TRT end-cap region is covered by 122,800 straw tubes aligned in radial direction. Each straw tube is filled with a Xe-based gas mixture, and a wire is placed at the center of the tube, acting as an anode. When a charged particle traverses the detector, it ionizes the gas mixture inside straws, producing a cascade of electrons. These electrons from the ionization drift toward the center wire, creating signal for the readout. The intrinsic resolution of a single straw tube is larger ($\sim 120\mu\text{m}$) than the silicon detectors [32], and a single straw tube do not provide information along the tube direction. However, time information² from large numbers of nearby TRT hits can be used to reconstruct the trajectory of a charged particle.

The TRT also provides important information on particle identification. The spaces between straws are filled with polymer fiber (barrels) and foils (end-caps) for the production

¹There are two versions of SCT strips in end-cap modules with lengths of 12 cm and 7 cm

²The signals from straw tubes are sampled in 24 time bins of 3.12 ns .

of transition radiation. When a highly relativistic charged particle passes through them, photons may be emitted by transition radiation, and these photons can be absorbed by the gas mixture, resulting in higher readout signals than usual, called high-threshold hits. The effect is stronger for electrons due to larger relativistic factor ($\gamma = E/m$) than particles with a lower boost such as hadrons. Therefore, the high-threshold hits in the TRT can be used for electron/pion identification [33].

2.2.2 The Calorimeters

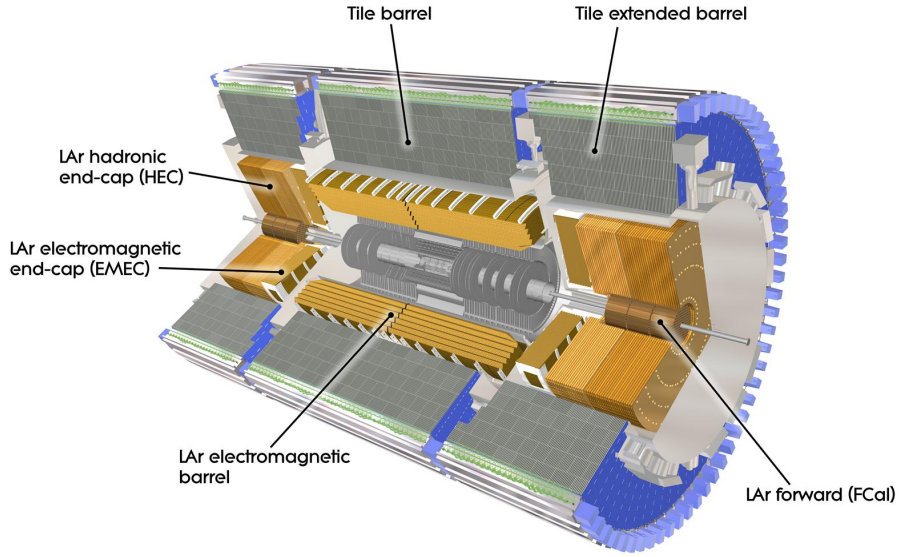


Figure 2.3: The ATLAS calorimeter system.

The ATLAS calorimetry system, shown in Figure 2.3, consists of two sub-systems, the Liquid Argon (LAr) calorimeters [34] and the Tile calorimeters (TileCals) [35]. The calorimeters are designed to measure the energy deposited by a particle as it traverse through the detector, and the signals from calorimeters are used for the Level 1 (L1) trigger system. Based on its usage, the calorimeters can be grouped into two sets of calorimeters: the Electromagnetic (EM) calorimeters and hadronic calorimeters.

Electromagnetic Calorimeter

The EM calorimeters (EMC) are located outside the ID and the solenoid magnet, and they are designed to measure the energy deposition from electrons and photons. They are composed of two LAr calorimeters, the EM End-Cap calorimeter (EMEC) covering the region of $|\eta| < 1.475$ and the EM Barrel (EMB) calorimeter covering the region of $1.375 < |\eta| < 3.2$. The LAr calorimeters are composed of layers of high density material (Pb) and LAr sampling layer interspaced for absorption of electron/photons and energy measurement, respectively. The first layer of the LAr calorimeters is called *presampler* which is a thin layer of liquid argon without absorber in front, and it is used to correct for the energy loss before a particle reach the calorimeter. The LAr calorimeters are called Sampling Calorimeters because only a small fraction of the deposited energy is measured by sampling layers.

When an electron or a photon enters the calorimeters, the electron/photon interacts with the absorber layers, creating the initial EM shower via bremsstrahlung and pair-production. The EM shower is amplified and collected by the sampling layers. The EM calorimeters have the minimum number of radiation length of $24 X_0$ [36].

Hadronic Calorimeter

Hadrons are less likely to produce bremsstrahlung radiation due to heavier mass, and they can traverse through the EMC without losing significant energy. Therefore, the hadronic calorimeters are located outside the EMC to measure the energy of hadrons penetrating the EMC. The hadron calorimeters are composed of both LAr calorimeters and TileCals.

The hadronic LAr calorimeters consists of two parts, the hadronic end-cap calorimeter (HEC) covering the region of $1.5 < |\eta| < 3.2$ and the forward calorimeter (FCAL) covering the region of $3.1 < |\eta| < 4.9$. The principal of hadronic LAr calorimeters is the same as EM LAr calorimeters. The HEC is divided into four longitudinal layers with copper absorber. The FCAL consists of one EM layer which uses copper as absorber and two hadronic layers with tungsten as passive material. When a hadron enters the hadronic LAr calorimeters, the particle interacts with nuclei of the absorber material via strong force, creating a hadronic shower. The hadronic shower is sampled by sampling layers.

TileCals are designed to cover the central barrel region ($|\eta| < 1.0$) and the extended barrel region ($0.8 < |\eta| < 1.7$). The TileCals are made of alternating layers of iron and scintillating tiles. Hadrons entering the absorber layers produce hadronic showers, and the secondary particles from the showers interact with the scintillating tiles to produce lights. The photons are delivered to photomultipliers via wave-length shifting fibers and registered as calorimeter

cluster hit.

The TileCals, combined with the hadronic LAr calorimeters, provide precise measurement of hadrons, jets, taus, and missing transverse energy (E_T^{miss}).

2.2.3 The Muon Spectrometer

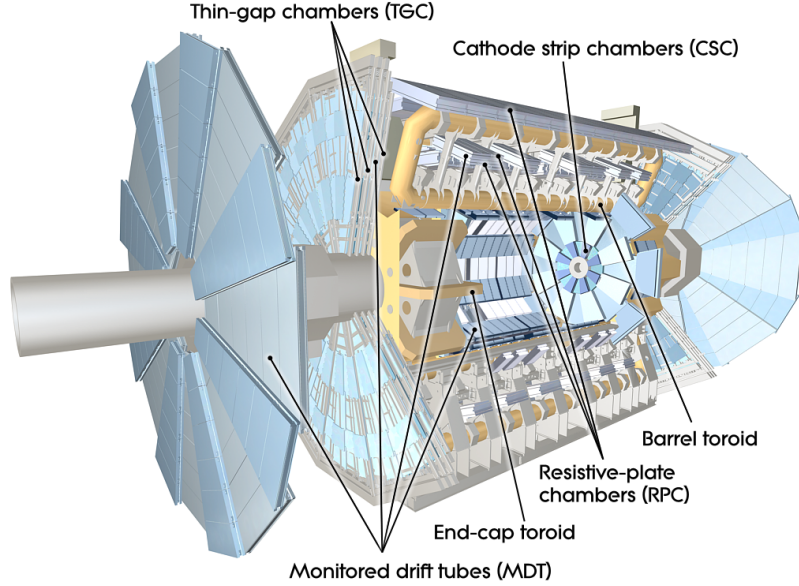


Figure 2.4: The ATLAS Muon Spectrometer

The Muon Spectrometer (MS) is the outermost detector in the ATLAS detector, responsible for muon identification, momentum measurements, and triggering of L1 Trigger. The MS is designed to provide high p_T momentum measurement with resolution of $\sigma_{p_T}/p_T = 10\%$, independent from the ID. The MS consists of four sub-detector systems. The Resistive Plate Chambers (RPCs) and the Thin Gap Chambers (TGCs) are used to trigger L1 Trigger. The Monitored Drift Tubes (MDTs) and the Cathode Strip Chambers (CSCs) allow precise tracking and momentum measurements. The MS barrel region covers the region of $|\eta| < 1$, and the coverage is extended to $|\eta| < 2.7$ in the end-cap. The magnetic field is applied with an average 0.5 T [37] by a system of a large toroidal magnet (barrel) and two smaller toroidal magnets (end-cap). A layout of the MS is shown in Figure 2.4.

Monitored Drift Tube Chambers

The MDT chambers provide precision momentum measurements using chambers of drift tubes filled with a gas mixture of Ar (97%) and CO₂(3%). The barrel MDT chambers are arranged in three layers, covering the region of $|\eta| < 1.1$. The end-cap MDT chambers are arranged in three wheels, covering the region of $1.1 < |\eta| < 2.7$. Each drift tubes measures 3 cm in a diameter, and a tungsten-rhenium wire is placed at the center as an anode. The layers and wheels have 6-8 layers of drift tubes with a space in between. The principal of particle detection is similar to the TRT, but the drift tubes are arranged perpendicular to the beam axis in the barrel layers and tangential in the end-cap layers. This configuration allows the MDT to measure the curvature of a muon in η - z plane under the toroidal magnetic field.

Cathode Strip Chambers

The CSCs are located on the innermost wheel of the end-caps, covering the region of $2.0 < |\eta| < 2.7$. In this region, the MDTs would not operate properly due to the high rates of muons coming from the beam pipe. Instead, sixteen CSCs on each end-cap provide precise tracking for high density muons with the resolution of 60 μm in η - z plane and 5 mm in the radial direction. The CSCs are multi-wire proportional chambers with segmented cathode strips in alternating alignment. The multi-wires are aligned in the radial direction, and the strips are aligned perpendicular or parallel to the wires to provide 2 dimensional measurements in both η and ϕ directions.

Resistive Plate Chambers

The RPCs provide trigger capability for the L1 muon trigger and measurements in η , ϕ coordinates in the barrel region. There are three RPCs arranged in concentric cylindrical shells around the beam axis. The two inner RPCs are placed at the radii of 5m and 7.5m to provide the low- p_T trigger information. The outer RPCs are installed at the radius of 10m to provide high- p_T trigger information. Each chamber consists of two parallel resistive plots separated by a 2 mm gap filled with a gas mixture based on C₂H₂F₄. A muon track passing through the RPCs ionizes the gas, and the signal is multiplied and read out by each chamber, providing 6 measurements for each track.

Thin Gap Chambers

The TGCs are designed to provide trigger information and ϕ measurements (non-bending direction) in the end-cap region. Similar to the CSCs, the TGCs are made of multi-wire proportional chambers filled with a gas mixture of 55% CO₂ and 45% C₅H₁₂. The strips are oriented in radial direction, allowing measurements in ϕ . The TGCs consists of 4 layers of chambers on each end-cap, covering the region of $1 < |\eta| < 2.7$.

2.2.4 The ATLAS Magnet

The ATLAS detector has three major superconducting magnet systems surrounding the ID and the MS: the Central Solenoid magnet and the Barrel/End-cap Toroid magnets.

Central Solenoid Magnet

The Central Solenoid magnet surrounds the ID, producing a 2 T magnetic field. The solenoid is designed to bend the trajectory of a charged particle in r - ϕ plane. The curvatures of charged particles are used for the measurements of charge-to-momentum ratio. The solenoid magnet measures 2.4 m in diameter and 5.3 m in length, and 7.73 kA of current is applied to generate the solenoidal magnetic field.

Toroid Magnets

In the outer region of the ATLAS detector, two superconducting toroid magnet systems are used to generate a magnetic field within the MS. The Barrel Toroid are composed of 8 separate coils made of Al/NbTi/Cu conductor with 120 turns. The toroid measures 20.1 m in diameter and 25.3 m in length. The End-cap Toroid has 8 coils with 116 turns, and the coils are made of the same material as the Barrel Toroid. The nominal current of 20.5 kA is applied to generate a magnetic field in the range of 1 to 2 T with the field integral between 2 to 8 Tm.

2.3 The ATLAS Trigger System

The ATLAS trigger system is designed to select interesting events from raw event data at high rate, generated by pp collisions. In Run 2, the LHC collide proton bunches every 25 ns, resulting in about a billion pp collisions per second at $\langle\mu\rangle = 24.9$ (in 2016). Due to the

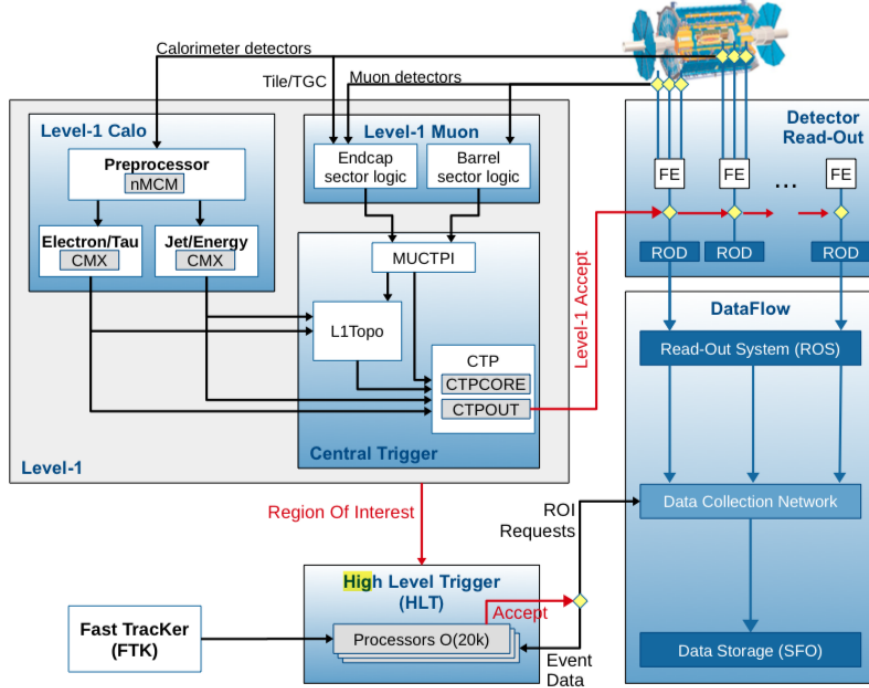


Figure 2.5: Layout of the ATLAS Trigger and data acquisition system in Run 2.

limited bandwidth and computing resources, it is impossible to record all events from the collisions. Therefore, the ATLAS trigger system is implemented to reduce the data taking rate from 40 MHz to 100 kHz. In Run 2, several upgrades have been performed in both hardware and software to maintain data quality in the environment with increasing pile-up, higher instantaneous luminosity at the center-of-mass energy of $\sqrt{s} = 13$ TeV.

The trigger system in Run 2 consists of a hardware-based Level 1 (L1) trigger and a software-based High Level Trigger (HLT). Figure 2.5 shows the ATLAS trigger and data acquisition system in Run 2. The events accepted by the trigger system are further processed by the Data Acquisition (DAQ) system where the information from front-end electronics of each detector component are used to build an individual event. The reconstructed events from DAQ are sent to Data Storage (SFO) for permanent storage.

2.3.1 Level 1 Trigger

The L1 trigger is a hardware-based trigger system that operates at the maximum rate of 100 kHz [38]. The main components of the L1 trigger consist of the L1 calorimeter trigger system and the L1 muon trigger system. The L1 trigger uses custom electronics to make

fast decisions and find regions of interest (RoI) in the detector, an important concept of the ATLAS trigger system, where potentially interesting activities are seen by the calorimeters or the MS.

A list of trigger selection from the L1 the HLT is developed based on the physics goal of the collaboration and the needs of individual analyses. The list is called the Trigger Menu [39]. The L1 trigger accepts the events with high p_T tracks, jets, or large E_T^{miss} that satisfies one of the trigger menu. The events accepted by the L1 trigger is passed to the HLT.

2.3.2 High Level Trigger

In Run 2, two software-based trigger systems, the Level 2 trigger and the Event Filter, are combined into a single software trigger system, called the High Level Trigger. The HLT makes the decision on events based on full information from the detector read-out in the RoI passed by the L1 trigger. This includes a fast reconstruction of the inner detector tracks. The HLT has the average output rate of 1 kHz [38], constrained by data storage limitation.

Chapter 3

Z' RECONSTRUCTION

The experimental signature in the search for long-lived Z' is characterized by a high- p_T dilepton vertex, displaced (>2 mm) from the primary vertex in transverse plane, referred a *displaced vertex*. In this chapter, the reconstruction of displaced vertices in the ATLAS Inner Detector is described.

3.1 Track Reconstruction in the Inner Detector

Track reconstruction in the ATLAS uses pattern recognition algorithms to reconstruct the trajectories of charged particles, referred as *track*. When a charged particle traverse through the ID, the particle interact with the sub-detectors of the ID (Pixel, SCT, and TRT), leaving raw detector signals. The raw signals are digitized and registered as detector *hits*, and these detector hits are used for track reconstruction.

3.1.1 Standard Tracking

The standard ATLAS track reconstruction is the main track reconstruction algorithm used in the ATLAS experiment. In the first stage of the track reconstruction, detector hits from the Pixel or the SCT detector are used to create *track seeds*, collections of silicon hits used for the initial track finding. If a track seed passes certain quality criteria, including a p_T and impact parameter selection, the track seed is extended to the outer part of the ID using a window search and pattern recognition algorithms. The extended tracks are evaluated based on p_T , number of hits, and impact parameters, and only the tracks satisfying the standard track selections are stored in the track collection. Figure 3.1 illustrates detector hits and reconstructed tracks in the ID. The important standard track selections is summarized in

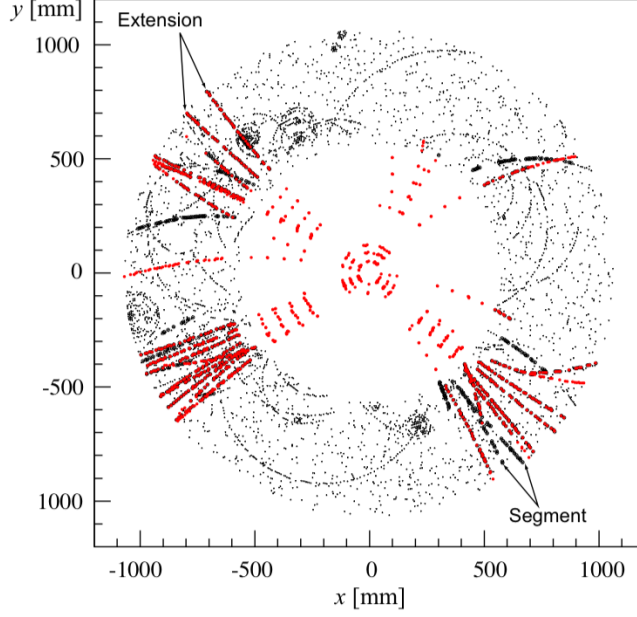


Figure 3.1: Illustration of detector hits and reconstructed tracks in the Inner Detector. The bright colors represent the detector hits associated with reconstructed tracks [1].

Table 3.1 [40].

Tracks are described by five parameters and a reference point, using a perigee representation. The parameters are the transverse (longitudinal) impact parameter d_0 (z_0), the azimuthal angle ϕ , the polar angle θ , and the charge-to-momentum ratio, q/p . The average position of the pp interaction, referred as beamspot, is used as the reference point for the track representation [41].

	Standard	Large radius
Maximum d_0 (mm)	10	300
Maximum z_0 (mm)	250	1500
Maximum $ \eta $	2.7	5
Maximum shared silicon modules	1	2
Minimum unshared silicon hits	6	5
Minimum silicon hits	7	7
Seed extension	Combinatorial	Sequential

Table 3.1: Important track selection in the standard and the large radius tracking algorithms.

3.1.2 Large Radius Tracking

The standard track reconstruction is proven to be very efficient in Run 2 with the tracking efficiency $> 90\%$ [42]. However, the tracking algorithm is optimized for primary charged particles promptly produced from pp collisions, and the strict requirements on the impact parameters, d_0 and z_0 potentially limit the tracking efficiency for the charged particles at large impact parameters ($d_0 > 2$ mm). Therefore, a dedicated track reconstruction algorithm, referred to as the large radius tracking (LRT), is developed to improve the track reconstruction efficiency for the tracks highly displaced from the primary vertex.

The LRT is performed in a sequence, following the standard tracking. It follows the same reconstruction strategy as the standard tracking, but there are a few importance difference between the standard tracking and the LRT.

- The pattern recognition algorithms in the LRT only uses *un-used* hits, the silicon hits that have not been used in the standard tracking, in creating and extending track candidates.
- The requirements on tracks such as d_0 , z_0 , and number of hits are relaxed.

The tracks satisfying certain criteria such as minimum p_T and number of detector hits are merged into the track collection from the standard track reconstruction. The track selections in the LRT are summarized and compared with the standard track reconstruction in Table 3.1. The combined track collection is used as an input for the lepton reconstruction and identification and secondary vertex reconstruction. More details on the large radius tracking can be found in Ref. [40].

Combined with the standard track reconstruction, the LRT provides overall technical efficiency of 90% or above for a displacement in the transverse plane up to 300 mm.

3.2 Electron Reconstruction

Electrons are characterized by energy deposits in the EM calorimeter and the associated reconstructed tracks in the ID. The electron reconstruction algorithm uses the energy deposits with total transverse energy > 2.5 GeV in a window size of 0.075×0.125 in (η, ϕ) to reconstruct EM clusters. The EM clusters are associated with tracks within the same RoI with the requirement $|\Delta\eta| < 0.05$ and $\Delta\phi$ where the effect of bremsstrahlung is taken into account. In the absence of a matching track, the EM cluster is classified as a photon candidate. The associated pairs of tracks and clusters are refitted to create electron candidates. Further

electron requirements, including likelihood-based identification criteria, are imposed to the electron candidates for reconstruction of electrons.

By default, electrons are required to have a minimum number of pixel hits and small transverse impact parameters. This is not optimal for the searches that aim to detect displaced vertices as the decay products of displaced vertices tend to have large impact parameters (d_0 , z_0) and missing hits in the inner layers of the detector. Therefore, these requirements are removed in this analysis.

3.3 Muon Reconstruction

Muons leave very small energy deposits in the calorimeter as they traverse through the detector due to the relatively larger mass, given that the probability of bremsstrahlung is $\propto 1/m^2$. However, they leave tracks in both the ID and the MS, referred as inner detector (ID) tracks and muon standalone (MS) tracks. The muon reconstruction algorithm uses MS tracks as seeds, and the MS tracks are extrapolated to the ID for the association with ID tracks. A *combined muon* track is created if a MS track is successfully associated with an ID track after the momentum correction for the energy loss from the interaction with the detector material. There are other types of reconstructed muons such as standalone muons, segment-tagged muons, and calorimeter-tagged muons [43]. However, these types of muons are not considered in this analysis as they do not have associated ID tracks which are required for the reconstruction of displaced vertices.

Similar to electrons, the requirements on a minimum number of pixel hits and minimum impact parameters (d_0 , z_0) are removed in this analysis.

3.4 Secondary Vertex Reconstruction

In the LHC, when two proton bunches collide, several different vertex topologies arise. The primary vertex and several pile-up vertices are formed along the beam line, and the vertices from photon conversion or long-lived particles are formed displaced from the primary vertex as shown in Figure 3.2. These displaced vertices are referred as secondary vertices. In the search for long-lived Z' in dilepton decay channel, the decay products of long-lived particles can be reconstructed as a secondary vertex.

The secondary vertex reconstruction is based on the algorithm developed for the primary vertex reconstruction [44]. In the first stage of the secondary vertex reconstruction, track are selected using the requirements on track parameters and hit patterns shown in Table 3.2.

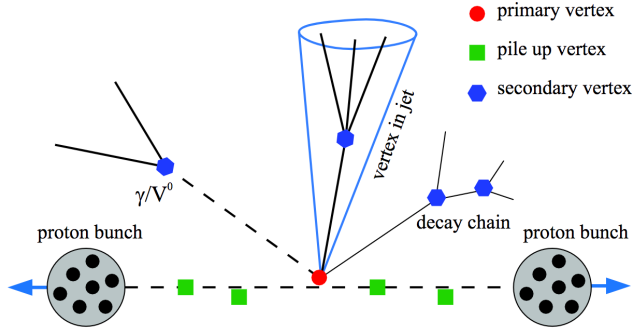


Figure 3.2: Important vertex topologies in pp collisions: primary, pile-up, and secondary vertices.

The tracks reconstructed by both the standard track reconstruction and the LRT are used as input. The tracks passing the track requirements are used to create two-track vertices, based on the closeness of two tracks in the space. This process results in a large number of fake vertices. The fake vertices are rejected by considering the location of a vertex and hit patterns of the tracks associated with the vertex. A vertex is rejected if the associated tracks have any hits at a radius smaller than the vertex position. Two-track vertices passing the fake rejection are refitted using a Kalman Filter for precise vertex position measurements, and track parameters are calculated with respect to the secondary vertex.

The two-track vertices reconstructed by the secondary vertex reconstruction serves as the primary analysis object in this thesis.

Variable	Cut
p_T (GeV)	> 1.0
χ^2/DOF	< 50.0
d_0 (mm)	$2.0 - 300.0$
z_0 (mm)	< 1500.0
SCT hits	≥ 2
Si shared hits	≤ 2
Pixel and TRT hits	TRT hits > 0 or Pixel hits ≥ 2

Table 3.2: Track requirements for secondary vertex reconstruction.

Chapter 4

ANALYSIS OVERVIEW

This thesis presents a search for a heavy long-lived resonance decaying to a dilepton pair, $\mu\mu$, ee , or $e\mu$ within the ATLAS Inner Detector. The analysis uses 32.8 fb^{-1} of pp collision data at $\sqrt{s} = 13 \text{ TeV}$ collected in 2016 in the ATLAS experiment. The long-lived particle (LLP) is referred as Z' but with no assumption on Z' production mechanism for a model-independent search.

There have been several searches for the LLPs produced in pp collisions in Run I at $\sqrt{s} = 8 \text{ TeV}$, including the search for displaced hadronic jet [45], displaced heavy flavors [46], or multi-track displaced vertex [47], and no significant excess was observed. The signature considered in this analysis is distinct from the previous searches, and it is one of the first efforts in the ATLAS experiment to search for a generic displaced vertex signature decaying to a dilepton pair. This analysis focuses on interpreting the LLPs decaying to displaced dilepton vertices in the context of model-independent, exotic resonance search.

In this search, a special setup (described in Section 3.1.2) of data reprocessing and reconstruction is used in order to gain sensitivity for the non-conventional signature of LLPs. The special setup allows the reconstruction of tracks with large impact parameters and secondary vertices significantly displaced from primary vertices.

Chapter 5

DATA AND MC SAMPLES

5.1 Data samples

The analysis uses the full 2016 pp collisions data (periods A-L) with the integrated luminosity of 32.8 fb^{-1} . In this search, because the standard ATLAS track reconstruction does not provide good sensitivity for long-lived particles, a dedicated stream, **DRAW_RPVLL**, is used to reconstruct events using the non-standard reconstruction as described in Chapter 3. The stream is used in several Exotics and SUSY analyses, searching for long-lived particles.

In **DRAW_RPVLL** stream, a subset of events from the main physics stream is selected by **RPVLL** filters. The filters select events using the HLT and offline selections configured for each analysis. The triggers and offline selection used in this search is discussed in Chapter ???. The selected events are passed downstream for reconstruction. The data is in **RAW** format so that low-level information such as detector hits can be used for the special reconstruction algorithms to reconstruct displaced tracks and vertices.

The events passing HLTs are processed in by a sequence of simulation and reconstruction algorithms with varying configurations, and the ATLAS metadata interface (AMI) tags are used to specify the configurations to be used for a data processing chain. In this analysis, the events are centrally processed with AMI tag **r8669** in which the dedicated track reconstruction algorithm, the large radius tracking, and the secondary vertex reconstruction algorithm are enabled to reconstruct displaced tracks and vertices, respectively. The output of **DRAW_RPVLL** stream is in **DAOD_RPVLL** format which is a standard **xAOD** data format with additional displaced tracks and secondary vertices reconstructed.

The **DAOD_RPVLL** is further processed to produce the **DAOD_SUSY15** derivation for the data

correction³ and reduction, as recommended by the Analysis Model Study Group (AMSG) [48]. Table 6.1 summarizes datasets used in this search.

Format	Dataset
DRAW_RPVLL	data16_13TeV.*.physics_Main.merge.DRAW_RPVLL.f*_m*
DAOD_RPVLL	data16_13TeV.*.physics_Main.recon.DAOD_RPVLL.f*_r8669
DAOD_SUSY15	data16_13TeV.*.physics_Main.recon.DAOD_RPVLL.f*_r8669_p2950

Table 5.1: Dataset used in DRAW_RPVLL, DAOD_RPVLL, and DAOD_SUSY15 format.

This search uses a modified version of the standard `GoodRunsList` because a small number of events selected by DRAW_RPVLL was not reconstructed successfully. The corresponding lumi blocks were removed from the `GoodRunsList`⁴.

5.2 MC samples

5.2.1 Signal samples

The long-lived Z' is generated using PYTHIA 6.4 [49] with the NNPDF23L0 PDF set and the min-bias tune A14. In this signal samples, Z' is singly produced from $q\bar{q}$ scattering and decays to a $\mu\mu$, ee , or $e\mu$ pair. The proper lifetime, $c\tau$, is set to 100 mm, 250 mm, or 500 mm. The mass of Z' is set between 100 and 1000 GeV. A width based on relativistic Breit-Wigner is assumed for the new resonance. A sample of 20k events are generated for each mass and lifetime. Table 6.2 summarizes dataset identifiers (DIDs), mass, width, and lifetime of the signal MC samples used in this search.

The signal MC samples generated using PYTHIA are processed to include detector simulation using the AMI tags `s2698` and `s2726`. The samples are overlaid with simulated minimum-bias events to model multiple interactions (pile-up) in data samples. In the signal MC samples, the average number of pile-ups, $\langle\mu\rangle$, ranges from 10 to 40 with small number of events having $\langle\mu\rangle < 10$. The difference in the $\langle\mu\rangle$ distributions between MC and data samples are corrected for by pile-up reweighting. The resulting MC samples are reconstructed using AMI tag `r8788`.

In the reconstruction process, the large radius tracking and the secondary vertex recon-

³Comes in the form of `AODfix`, centrally released by the ATLAS collaboration.

⁴`data16_13TeV.periodAllYear_DetStatus-v83-pro20-15_DQDefects-00-02-04_PHYS_StandardGRL_All_Good\25ns-DAOD_RPVLL_r8669.xml`

$m_{Z'}$ (GeV)	Γ (GeV)	$c\tau$ (mm)	DID		
			$\mu\mu$	ee	$e\mu$
100	2.8	100	308264	-	-
100	2.8	250	308265	-	-
100	2.8	500	308266	-	-
250	6.9	100	301911	-	-
250	6.9	250	301912	-	-
250	6.9	500	301913	-	-
500	14.7	100	301914	-	-
500	14.7	250	301915	-	-
500	14.7	500	301916	-	-
750	23.0	100	308285	-	-
750	23.0	250	308286	-	-
750	23.0	500	308287	-	-
1000	31.0	100	301917	-	-
1000	31.0	250	301918	-	-
1000	31.0	500	301919	-	-

Table 5.2: Mass, lifetime, and DID of the signal MC samples.

struction algorithms are used with the same configuration as data samples to reconstruct displaced tracks and vertices. The reconstructed events are stored in DAOD_RPVLL, and the samples are processed to produce the DAOD_SUSY15 derivation for data reduction and the correction.

The representative plots of truth-level p_T and η distributions of Z' and the muons from the decay of Z' , referred as *signal* muons, are shown in Figure 6.1 using the signal MC samples with $m = 500, 1000$ GeV and $c\tau = 100$ mm. The signal MC samples with ee and $e\mu$ final states produce similar distributions as shown in Appendix A.

The η distribution of signal muons shows that most of the signal muons are produced within the detector acceptance ($\eta < 2.7$). The characteristic upper edge in the p_T spectrum is related to the Z' mass.

5.2.2 Background MC samples

In this analysis, backgrounds are estimated from data because most of the backgrounds are expected to be originated from non-collision processes such as cosmic rays or random-crossing of tracks.

However, SM background samples are used to study the performance of random-crossing

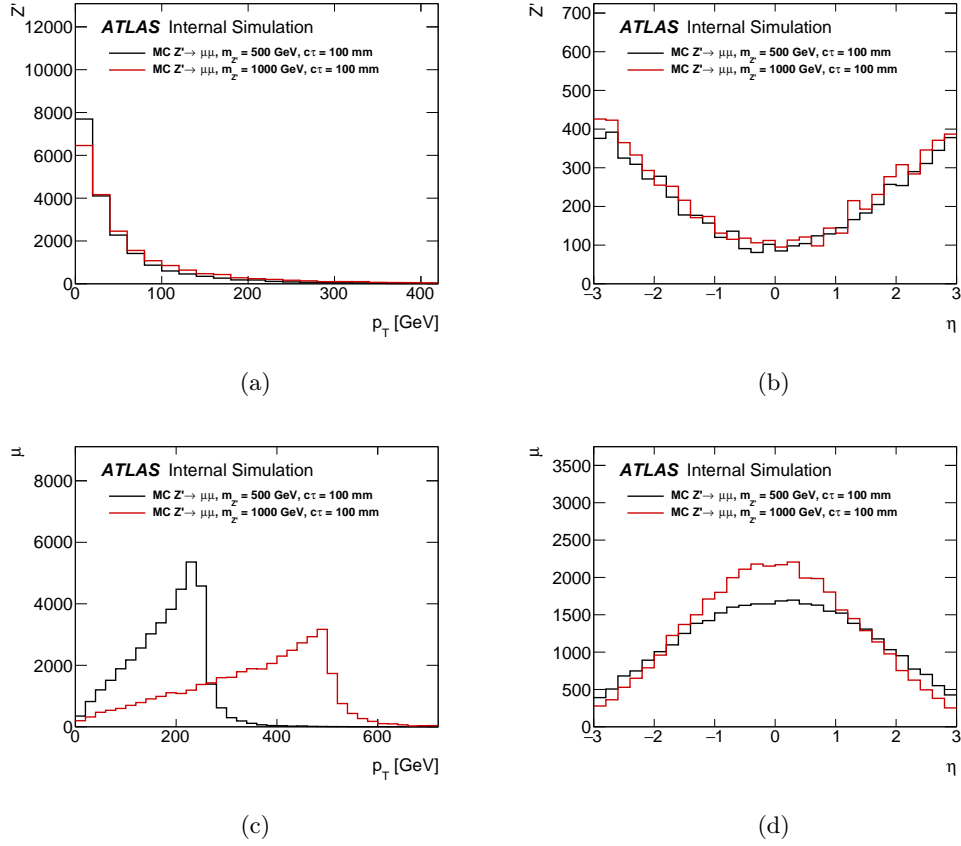


Figure 5.1: The representative plots of truth-level (a) p_T and (b) η distributions of Z' , and (c), (d) are the corresponding distributions for the signal muons. The signal MC samples are generated with $m = 500, 1000$ GeV, and $c\tau = 100$ mm.

background estimation (Section 7.1) and to estimate the systematic uncertainties in vertexing and tracking (Section 8.1). The $t\bar{t}$ samples are generated for QCD background using **SHERPA** with the **NNPDF30NNLO** PDF set. The samples with leptonic decay of di-boson (ZZ , WW , $W^\pm Z$) are generated using **SHERPA** with the **CT10** PDF set, and the dijet samples are generated using **PYTHIA8** with **NNPDF23LO** PDF set for their large lepton population.

The SM background samples are reprocessed using the same configuration as the signal MC sample for consistency. The background MC samples used for background and systematic uncertainty estimations are summarized in Table 6.3.

Process	DID	σ (pb)	Events (10^6)	$\mathcal{L}_{Int}(\text{fb}^{-1})$
$t\bar{t}$	410252	87.8	0.70	7.97
$ZZ \rightarrow \ell\ell\ell\ell$	361063	11.7	0.12	10.3
$W^- Z \rightarrow \ell\ell\ell\nu$	361064	1.68	0.020	10.2
$W^+ Z \rightarrow \ell\ell\ell\nu$	361066	2.33	0.70	30.0
$WW \rightarrow \ell\ell\nu\nu$	361068	12.8	0.025	1.95
JZ3W	361023	$8.45 \cdot 10^3$	0.20	0.0247
JZ4W	361024	135	0.20	1.48
JZ5W	361025	4.20	0.20	47.6
JZ6W	361026	$2.42 \cdot 10^{-2}$	0.20	826

Table 5.3: Background MC samples used in the study of random-crossing background and in the estimation of tracking and vertexing systematic uncertainty.

Chapter 6

DATA AND MC SAMPLES

6.1 Data samples

The analysis uses the full 2016 pp collisions data (periods A-L) with the integrated luminosity of 32.8 fb^{-1} . In this search, because the standard ATLAS track reconstruction does not provide good sensitivity for long-lived particles, a dedicated stream, **DRAW_RPVLL**, is used to reconstruct events using the non-standard reconstruction as described in Chapter 3. The stream is used in several Exotics and SUSY analyses, searching for long-lived particles.

In **DRAW_RPVLL** stream, a subset of events from the main physics stream is selected by **RPVLL** filters. The filters select events using the HLT and offline selections configured for each analysis. The triggers and offline selection used in this search is discussed in Chapter ???. The selected events are passed downstream for reconstruction. The data is in **RAW** format so that low-level information such as detector hits can be used for the special reconstruction algorithms to reconstruct displaced tracks and vertices.

The events passing HLTs are processed in by a sequence of simulation and reconstruction algorithms with varying configurations, and the ATLAS metadata interface (AMI) tags are used to specify the configurations to be used for a data processing chain. In this analysis, the events are centrally processed with AMI tag **r8669** in which the dedicated track reconstruction algorithm, the large radius tracking, and the secondary vertex reconstruction algorithm are enabled to reconstruct displaced tracks and vertices, respectively. The output of **DRAW_RPVLL** stream is in **DAOD_RPVLL** format which is a standard **xAOD** data format with additional displaced tracks and secondary vertices reconstructed.

The **DAOD_RPVLL** is further processed to produce the **DAOD_SUSY15** derivation for the data

correction⁵ and reduction, as recommended by the Analysis Model Study Group (AMSG) [48]. Table 6.1 summarizes datasets used in this search.

Format	Dataset
DRAW_RPVLL	data16_13TeV.*.physics_Main.merge.DRAW_RPVLL.f*_m*
DAOD_RPVLL	data16_13TeV.*.physics_Main.recon.DAOD_RPVLL.f*_r8669
DAOD_SUSY15	data16_13TeV.*.physics_Main.recon.DAOD_RPVLL.f*_r8669_p2950

Table 6.1: Dataset used in DRAW_RPVLL, DAOD_RPVLL, and DAOD_SUSY15 format.

This search uses a modified version of the standard `GoodRunsList` because a small number of events selected by DRAW_RPVLL was not reconstructed successfully. The corresponding lumi blocks were removed from the `GoodRunsList`⁶.

6.2 MC samples

6.2.1 Signal samples

The long-lived Z' is generated using PYTHIA 6.4 [49] with the NNPDF23L0 PDF set and the min-bias tune A14. In this signal samples, Z' is singly produced from $q\bar{q}$ scattering and decays to a $\mu\mu$, ee , or $e\mu$ pair. The proper lifetime, $c\tau$, is set to 100 mm, 250 mm, or 500 mm. The mass of Z' is set between 100 and 1000 GeV. A width based on relativistic Breit-Wigner is assumed for the new resonance. A sample of 20k events are generated for each mass and lifetime. Table 6.2 summarizes dataset identifiers (DIDs), mass, width, and lifetime of the signal MC samples used in this search.

The signal MC samples generated using PYTHIA are processed to include detector simulation using the AMI tags `s2698` and `s2726`. The samples are overlaid with simulated minimum-bias events to model multiple interactions (pile-up) in data samples. In the signal MC samples, the average number of pile-ups, $\langle\mu\rangle$, ranges from 10 to 40 with small number of events having $\langle\mu\rangle < 10$. The difference in the $\langle\mu\rangle$ distributions between MC and data samples are corrected for by pile-up reweighting. The resulting MC samples are reconstructed using AMI tag `r8788`.

In the reconstruction process, the large radius tracking and the secondary vertex recon-

⁵Comes in the form of `AODfix`, centrally released by the ATLAS collaboration.

⁶`data16_13TeV.periodAllYear_DetStatus-v83-pro20-15_DQDefects-00-02-04_PHYS_StandardGRL_All_Good\25ns-DAOD_RPVLL_r8669.xml`

$m_{Z'}$ (GeV)	Γ (GeV)	$c\tau$ (mm)	DID		
			$\mu\mu$	ee	$e\mu$
100	2.8	100	308264	-	-
100	2.8	250	308265	-	-
100	2.8	500	308266	-	-
250	6.9	100	301911	-	-
250	6.9	250	301912	-	-
250	6.9	500	301913	-	-
500	14.7	100	301914	-	-
500	14.7	250	301915	-	-
500	14.7	500	301916	-	-
750	23.0	100	308285	-	-
750	23.0	250	308286	-	-
750	23.0	500	308287	-	-
1000	31.0	100	301917	-	-
1000	31.0	250	301918	-	-
1000	31.0	500	301919	-	-

Table 6.2: Mass, lifetime, and DID of the signal MC samples.

struction algorithms are used with the same configuration as data samples to reconstruct displaced tracks and vertices. The reconstructed events are stored in DAOD_RPVLL, and the samples are processed to produce the DAOD_SUSY15 derivation for data reduction and the correction.

The representative plots of truth-level p_T and η distributions of Z' and the muons from the decay of Z' , referred as *signal* muons, are shown in Figure 6.1 using the signal MC samples with $m = 500, 1000$ GeV and $c\tau = 100$ mm. The signal MC samples with ee and $e\mu$ final states produce similar distributions as shown in Appendix A.

The η distribution of signal muons shows that most of the signal muons are produced within the detector acceptance ($\eta < 2.7$). The characteristic upper edge in the p_T spectrum is related to the Z' mass.

6.2.2 Background MC samples

In this analysis, backgrounds are estimated from data because most of the backgrounds are expected to be originated from non-collision processes such as cosmic rays or random-crossing of tracks.

However, SM background samples are used to study the performance of random-crossing

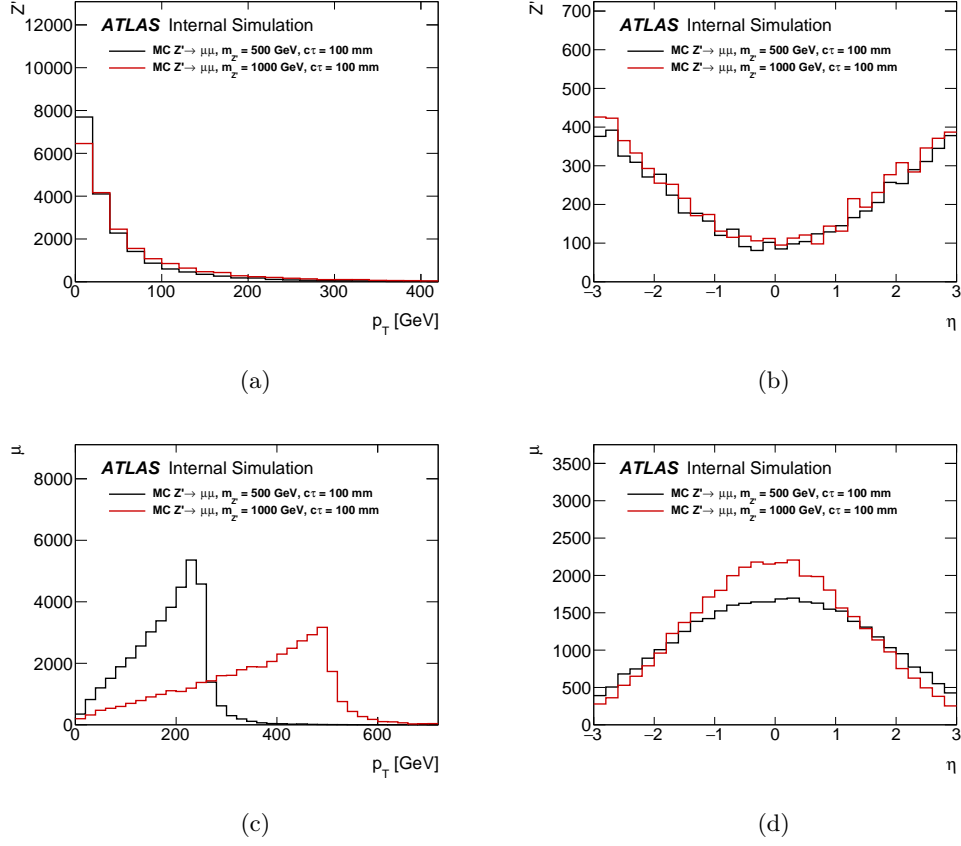


Figure 6.1: The representative plots of truth-level (a) p_T and (b) η distributions of Z' , and (c), (d) are the corresponding distributions for the signal muons. The signal MC samples are generated with $m = 500, 1000$ GeV, and $c\tau = 100$ mm.

background estimation (Section 7.1) and to estimate the systematic uncertainties in vertexing and tracking (Section 8.1). The $t\bar{t}$ samples are generated for QCD background using **SHERPA** with the **NNPDF30NNLO** PDF set. The samples with leptonic decay of di-boson (ZZ , WW , $W^\pm Z$) are generated using **SHERPA** with the **CT10** PDF set, and the dijet samples are generated using **PYTHIA8** with **NNPDF23LO** PDF set for their large lepton population.

The SM background samples are reprocessed using the same configuration as the signal MC sample for consistency. The background MC samples used for background and systematic uncertainty estimations are summarized in Table 6.3.

Process	DID	σ (pb)	Events (10^6)	$\mathcal{L}_{Int}(\text{fb}^{-1})$
$t\bar{t}$	410252	87.8	0.70	7.97
$ZZ \rightarrow \ell\ell\ell\ell$	361063	11.7	0.12	10.3
$W^- Z \rightarrow \ell\ell\ell\nu$	361064	1.68	0.020	10.2
$W^+ Z \rightarrow \ell\ell\ell\nu$	361066	2.33	0.70	30.0
$WW \rightarrow \ell\ell\nu\nu$	361068	12.8	0.025	1.95
JZ3W	361023	$8.45 \cdot 10^3$	0.20	0.0247
JZ4W	361024	135	0.20	1.48
JZ5W	361025	4.20	0.20	47.6
JZ6W	361026	$2.42 \cdot 10^{-2}$	0.20	826

Table 6.3: Background MC samples used in the study of random-crossing background and in the estimation of tracking and vertexing systematic uncertainty.

Chapter 7

BACKGROUND ESTIMATION

7.1 Random-Crossing Background

Chapter 8

SYSTEMATIC UNCERTAINTIES

8.1 Systematics in Vertexing and Tracking

BIBLIOGRAPHY

- [1] T. Cornelissen, M. Elsing, I. Gavrilenko, W. Liebig, E. Moyse, and A. Salzburger, “The new atlas track reconstruction (newt),” *Journal of Physics: Conference Series*, vol. 119, no. 3, p. 032014, 2008.
- [2] C. P. Burgess and G. D. Moore, *The standard model: A primer*. Cambridge University Press, 2006.
- [3] P. W. Higgs, “Broken Symmetries and the Masses of Gauge Bosons,” *Phys. Rev. Lett.*, vol. 13, pp. 508–509, 1964.
- [4] M. Kobayashi and T. Maskawa, “Cp-violation in the renormalizable theory of weak interaction,” *Progress of Theoretical Physics*, vol. 49, no. 2, pp. 652–657, 1973.
- [5] H. Suganuma, S. Sasaki, and H. Toki, “Color confinement, quark pair creation and dynamical chiral-symmetry breaking in the dual ginzburg-landau theory,” *Nuclear Physics B*, vol. 435, no. 1, pp. 207 – 240, 1995.
- [6] P. W. Higgs, “Broken symmetries and the masses of gauge bosons,” *Phys. Rev. Lett.*, vol. 13, pp. 508–509, Oct 1964.
- [7] V. A. Kostelecký, “Gravity, lorentz violation, and the standard model,” *Phys. Rev. D*, vol. 69, p. 105009, May 2004.
- [8] N. A. Hamed, S. Dimopoulos, and G. Dvali, “The hierarchy problem and new dimensions at a millimeter,” *Physics Letters B*, vol. 429, no. 3, pp. 263 – 272, 1998.
- [9] M. Magg and C. Wetterich, “Neutrino mass problem and gauge hierarchy,” *Physics Letters B*, vol. 94, no. 1, pp. 61 – 64, 1980.
- [10] J. F. Navarro, “The structure of cold dark matter halos,” in *Symposium-international astronomical union*, vol. 171, pp. 255–258, Cambridge University Press, 1996.
- [11] G. Bertone, D. Hooper, and J. Silk, “Particle dark matter: Evidence, candidates and constraints,” *Physics Reports*, vol. 405, no. 5, pp. 279–390, 2005.

- [12] D. Clowe, M. Bradač, A. H. Gonzalez, M. Markevitch, S. W. Randall, C. Jones, and D. Zaritsky, “A direct empirical proof of the existence of dark matter,” *The Astrophysical Journal Letters*, vol. 648, no. 2, p. L109, 2006.
- [13] M. Ahn, S. Aoki, H. Bhang, S. Boyd, D. Casper, J. Choi, S. Fukuda, Y. Fukuda, W. Gajewski, T. Hara, *et al.*, “Indications of neutrino oscillation in a 250 km long-baseline experiment,” *Physical Review Letters*, vol. 90, no. 4, p. 041801, 2003.
- [14] S. Mikheev and A. Y. Smirnov, “Resonance amplification of oscillations in matter and spectroscopy of solar neutrinos,” *Yadernaya Fizika*, vol. 42, no. 6, pp. 1441–1448, 1985.
- [15] D. Toussaint, S. Treiman, F. Wilczek, and A. Zee, “Matter-antimatter accounting, thermodynamics, and black-hole radiation,” *Physical Review D*, vol. 19, no. 4, p. 1036, 1979.
- [16] M. Dine and A. Kusenko, “Origin of the matter-antimatter asymmetry,” *Reviews of Modern Physics*, vol. 76, no. 1, p. 1, 2003.
- [17] M. J. Strassler and K. M. Zurek, “Echoes of a hidden valley at hadron colliders,” *Physics Letters B*, vol. 651, no. 5, pp. 374–379, 2007.
- [18] S. Cassel, D. Ghilencea, and G. Ross, “Electroweak and dark matter constraints on a z' in models with a hidden valley,” *Nuclear Physics B*, vol. 827, no. 1, pp. 256–280, 2010.
- [19] G. Senjanovic and R. N. Mohapatra, “Exact left-right symmetry and spontaneous violation of parity,” *Physical Review D*, vol. 12, no. 5, p. 1502, 1975.
- [20] R. N. Mohapatra and G. Senjanović, “Neutrino masses and mixings in gauge models with spontaneous parity violation,” *Physical Review D*, vol. 23, no. 1, p. 165, 1981.
- [21] L. Basso, A. Belyaev, S. Moretti, and C. H. Shepherd-Themistocleous, “Phenomenology of the minimal B-L extension of the Standard model: Z' and neutrinos,” *Phys. Rev.*, vol. D80, p. 055030, 2009.
- [22] P. Langacker, “The Physics of Heavy Z' Gauge Bosons,” *Rev. Mod. Phys.*, vol. 81, pp. 1199–1228, 2009.
- [23] V. Barger, W. Keung, and E. Ma, “Sequential w and z bosons,” *Physics Letters B*, vol. 94, no. 3, pp. 377 – 380, 1980.
- [24] Q.-H. Cao, Z. Li, J.-H. Yu, and C.-P. Yuan, “Discovery and identification of W' and Z' in $su(2)_1 \otimes su(2)_2 \otimes u(1)_X$ models at the lhc,” *Phys. Rev. D*, vol. 86, p. 095010, Nov 2012.
- [25] “Search for a heavy neutral gauge boson in the dielectron channel with 5.4 fb^{-1} of $p\bar{p}$ collisions at $s=1.96 \text{ tev}$,” *Physics Letters B*, vol. 695, no. 1, pp. 88 – 94, 2011.
- [26] “Search for high-mass dilepton resonances in pp collisions at $\sqrt{s} = 8 \text{ TeV}$ with the atlas detector,” *Phys. Rev. D*, vol. 90, p. 052005, Sep 2014.
- [27] I. R. Kenyon, “The drell-yan process,” *Reports on Progress in Physics*, vol. 45, no. 11, p. 1261, 1982.

- [28] P. Langacker, “Z’ Physics at the LHC,” 2009.
- [29] O. S. Bråijning, P. Collier, P. Lebrun, S. Myers, R. Ostojic, J. Poole, and P. Proudlock, *LHC Design Report*. CERN Yellow Reports: Monographs, Geneva: CERN, 2004.
- [30] H. Pernegger, “The pixel detector of the atlas experiment for lh run-2,” *Journal of Instrumentation*, vol. 10, no. 06, p. C06012, 2015.
- [31] F. Hüggling and Atlas Collaboration, “The ATLAS Pixel Insertable B-layer (IBL),” *Nuclear Instruments and Methods in Physics Research A*, vol. 650, pp. 45–49, Sept. 2011.
- [32] A. Vogel, “ATLAS Transition Radiation Tracker (TRT): Straw Tube Gaseous Detectors at High Rates,” Tech. Rep. ATL-INDET-PROC-2013-005, CERN, Geneva, Apr 2013.
- [33] “Particle Identification Performance of the ATLAS Transition Radiation Tracker,” Tech. Rep. ATLAS-CONF-2011-128, CERN, Geneva, Sep 2011.
- [34] H. Zhang and the ATLAS Liquid Argon Calorimeter Group, “The atlas liquid argon calorimeter: Overview and performance,” *Journal of Physics: Conference Series*, vol. 293, no. 1, p. 012044, 2011.
- [35] A. M. Henriques Correia, “The ATLAS Tile Calorimeter,” Tech. Rep. ATL-TILECAL-PROC-2015-002, CERN, Geneva, Mar 2015.
- [36] *ATLAS liquid-argon calorimeter: Technical Design Report*. Technical Design Report ATLAS, Geneva: CERN, 1996.
- [37] M. Arnaud, J. Bardoux, F. Bergsma, G. Bobbink, A. Bruni, L. Chevalier, P. Ennes, P. Fleischmann, M. Fontaine, A. Formica, V. Gautard, H. Groenstege, C. Guyot, R. Hart, W. Kozanecki, P. Iengo, M. Legendre, T. Nikitina, E. Perepelkin, P. Ponsot, A. Richardson, A. Vorozhtsov, and S. Vorozhtsov, “Commissioning of the magnetic field in the atlas muon spectrometer,” *Nuclear Physics B - Proceedings Supplements*, vol. 177-178, pp. 265 – 266, 2008. Proceedings of the Hadron Collider Physics Symposium 2007.
- [38] A. R. Martínez García and A. Collaboration, “The run-2 atlas trigger system,” *Journal of Physics: Conference Series*, vol. 762, no. 1, p. 012003, 2016.
- [39] T. Vazquez Schroeder, “The ATLAS Trigger in Run-2: Design, Menu, and Performance,” Tech. Rep. ATL-DAQ-PROC-2017-027, CERN, Geneva, Oct 2017.
- [40] “Performance of the reconstruction of large impact parameter tracks in the ATLAS inner detector,” Tech. Rep. ATL-PHYS-PUB-2017-014, CERN, Geneva, Jul 2017.
- [41] M. Aaboud *et al.*, “Reconstruction of primary vertices at the ATLAS experiment in Run 1 proton–proton collisions at the LHC,” *Eur. Phys. J.*, vol. C77, no. 5, p. 332, 2017.
- [42] M. Aaboud *et al.*, “Performance of the ATLAS Track Reconstruction Algorithms in Dense Environments in LHC Run 2,” *Eur. Phys. J.*, vol. C77, no. 10, p. 673, 2017.
- [43] G. Aad *et al.*, “Muon reconstruction performance of the ATLAS detector in proton–proton collision data at $\sqrt{s}=13$ TeV,” *Eur. Phys. J.*, vol. C76, no. 5, p. 292, 2016.

- [44] G. Piacquadio, K. Prokofiev, and A. Wildauer, “Primary vertex reconstruction in the atlas experiment at lh_c,” *Journal of Physics: Conference Series*, vol. 119, no. 3, p. 032033, 2008.
- [45] D. Blackburn, B. Brau, A. Coccaro, H. Lubatti, P. Pais, E. Pueschel, H. Russell, and D. Ventura, “Search for long-lived, weakly-interacting particle that decay to displaced hadronic jets in proton-proton collisions at $\sqrt{s} = 8$ TeV with the ATLAS detector,” Tech. Rep. ATL-COM-PHYS-2013-683, CERN, Geneva, May 2013.
- [46] O. Harris, H. Lubatti, A. Mastroberardino, R. Rosten, D. Salvatore, G. Susinno, M. Verducci, and G. Watts, “Searches for long-lived neutral particles decaying into heavy flavors in the hadronic calorimeter of ATLAS at $\sqrt{s} = 8$ TeV,” Tech. Rep. ATL-COM-PHYS-2013-113, CERN, Geneva, Feb 2013. EdBoard for EXOT-2012-28: Shlomit Tarem, Irene Vichou, Claudia Gemme, Masahiro Kuze.
- [47] G. Aad *et al.*, “Search for massive, long-lived particles using multitrack displaced vertices or displaced lepton pairs in pp collisions at $\sqrt{s} = 8$ TeV with the ATLAS detector,” *Phys. Rev.*, vol. D92, no. 7, p. 072004, 2015.
- [48] J. Catmore, M. Elsing, E. Lipeles, D. Rousseau, and I. Vivarelli, “Report of the Analysis Model Study Group,” Tech. Rep. ATL-COM-SOFT-2013-005, CERN, Geneva, Apr 2013.
- [49] T. Sjöstrand, S. Mrenna, and P. Skands, “Pythia 6.4 physics and manual,” *Journal of High Energy Physics*, vol. 2006, no. 05, p. 026, 2006.

A Truth-level p_T and η distributions of Signal MC samples

This appendix contains ...